Robotica (2025), **43**, pp. 3419–3441
doi:10.1017/S0263574725102300

CAMBRIDGE UNIVERSITY PRESS

RESEARCH ARTICLE

Human–machine coupling dynamics modeling and adaptive admittance control of lower limb rehabilitation robot

Chao Gao[1], Chang Wang[2], Hui Li[2], Jianhua Zhang[2], Xinpeng Du[1] and Jianjun Zhang[1]

[1]School of Mechanical Engineering, Hebei University of Technology, Tianjin, China
[2]School of Mechanical Engineering, University of Science and Technology Beijing, Beijing, China
Corresponding author: Hui Li; Email: 15704965986@163.com

Received: 7 April 2025; **Revised:** 17 July 2025; **Accepted:** 2 August 2025; **First published online:** 24 September 2025

Keywords: lower limb rehabilitation robot; human–machine coupling; nonlinear system; dynamic model; adaptive control

Abstract

Human–machine compatibility and collaborative control for stroke patients utilizing lower limb rehabilitation robots have attracted considerable research attention. As a highly human–machine-coupled system, ensuring adequate compliance and safety is fundamental to efficient and comfortable rehabilitation. Therefore, this paper first quantifies human–machine contact interactions, proposes a human–machine coupling dynamics modeling method, and identifies the robot's dynamic inertia parameters and human lower limb parameters. Second, a dual closed-loop controller for the rehabilitation robot is designed. Based on the bottom position control, an adaptive admittance control algorithm is proposed that employs the root-mean-square propagation (RMSprop) algorithm to tune the adaptive gain. In rehabilitation training, the controller can adaptively adjust the admittance parameters according to the human–machine interaction force to achieve responsiveness to the dynamic changes of the human–machine system. The experimental results of the control system show that the human–machine cooperative control performance is significantly improved, the maximum joint angle error is reduced by more than 40.9%, and the maximum human–machine interaction force is reduced by more than 19.4%.

1. Introduction

Asia, the world's most populous region, is home to approximately 9.5–10.6 million stroke patients annually [1]. Stroke, as a non-communicable disease, and particularly in China, has established itself as one of the leading causes of death and disability among older adults [2]. Compared with traditional physical, occupational, and language therapy, robot-assisted rehabilitation technology offers three primary advantages in stroke rehabilitation. First, precise motion control capability: The robot achieves precise motion positioning through an optical encoder and closed-loop control, reducing subjective errors in traditional manipulation [3, 4]. Second, a standardized training system: The technology features built-in switchable training modes (e.g., virtual scene interaction, resistance training). Real-time calibration of joint trajectories via sensors, combined with closed-loop algorithms, ensures significantly higher standardization of training actions than traditional methods [5, 6]. Third, a quantitative evaluation system: Rehabilitation robots can collect core data such as joint activity and gait spatio-temporal parameters (e.g., step length, step frequency) through a sensor network. Based on an AI algorithm, they generate real-time dynamic rehabilitation reports with motor function trends, enhancing the objectivity of therapeutic effect evaluation by 50%–60% compared to traditional manual assessments [7]. According to prior research, various lower limb rehabilitation robots (e.g., Lokomat, HAL, Ekso) have been evaluated in clinical trials at multiple global research centers [8]. Numerous RCTs have demonstrated that robot-assisted rehabilitation

© The Author(s), 2025. Published by Cambridge University Press.

https://doi.org/10.1017/S0263574725102300 Published online by Cambridge University Press

outperforms traditional therapy in improving gait independence and long-term outcomes [9, 10]. More importantly, in the field of stroke rehabilitation, robot-assisted gait rehabilitation (RAGT) has been recommended as an essential adjuvant therapy by multiple international clinical guidelines (e.g., American Heart Association, Canadian Stroke Guidelines) and consequently has gradually emerged as a common clinical intervention [11]. However, varying brain injuries among patients (including lesion location, size, and concomitant neurological deficits) drive clinical heterogeneity. Specifically, prefrontal and parietal lobe damage may impair cognitive functions, while primary motor cortex (M1) lesions disrupt limb motor abilities [12]. These anatomical and functional heterogeneities directly determine residual limb motor capacity, influencing neural plasticity and training adaptability. Thus, rehabilitation strategies (including exoskeleton assistance strength, step frequency parameters, and task-oriented training protocols) require dynamic adjustment based on individual injury profiles [13].

Diverse lower-limb rehabilitation robots have been developed to meet the varied needs of rehabilitation training for lower-limb movement disorders [14]. Motion Maker, a representative lower-limb rehabilitation robot, was developed by the Swiss Federal Institute of Technology [15]. The robot has bilateral mechanical exoskeleton legs, which can perform lower-limb rehabilitation training in horizontal lying, inclined lying, and sitting postures. The Lokomat lower-limb rehabilitation robot developed by Hocoma (Switzerland) [16] has a global installation base of approximately 1,200 units. However, its widespread clinical adoption has been hindered by its bulky mechanical design, high cost, and restriction to standing gait training. The multi-joint lower-limb rehabilitation robot developed by Yanshan University [17, 18] – capable of enabling both active and passive lower limb training in sitting and recumbent postures – has successfully entered the rehabilitation departments of multiple hospitals [19].

Overall, there have been substantial advancements in lower-limb rehabilitation robots. However, the industrialization process remains protracted. Although these commercial products have certain technological advancements, they have revealed practical limitations such as insufficient adaptability to different patient states and poor flexibility in human–computer interaction in clinical applications [20]. These limitations reflect the technical bottlenecks of robot systems in adaptability and flexibility of human–machine cooperative control [21]. The key to enhancing the adaptability of rehabilitation robot systems to patients lies in adequately accounting for human–machine contact interaction [22] and establishing an accurate human–machine dynamics model [23, 24]. Solving the problem of human–machine collaborative control compliance – and thereby enhancing rehabilitation comfort [25] and training effectiveness – relies on stable and reliable control methodologies. Widely adopted control approaches include PID control, impedance control, and admittance control [26–29]. In ref. [30], Aguirre-Ollinger et al. analyzed the effect of 1-DOF exoskeleton admittance control. Experimental results demonstrate an improvement in the robot's compliance. Chen et al. [31] employed admittance control to map human–robot interaction forces to desired trajectories, thereby achieving the robot's active compliance with human lower limbs. However, in clinical practice, patients may experience muscle spasms, abnormal gait patterns, and other complications, potentially leading to mechanical compression or secondary injuries during human–robot interaction. Therefore, the aforementioned control method cannot accommodate the strongly nonlinear dynamics of human–machine coupling. To address this limitation, a feedforward control strategy is introduced [32], with compliance control parameters adjusted in real time based on human–machine interaction forces [33]. This enables dynamic adaptation, thereby enhancing the performance of human–machine cooperative control.

This paper takes the multi-posture lower-limb rehabilitation robot as the research object. The contact interaction is systematically analyzed and quantified to establish a human–machine coupling dynamics model. Building upon a low-level position controller, an admittance controller that takes human–machine contact force as its input is designed, employing the RMSprop adaptive algorithm to achieve adaptive control of the lower-limb rehabilitation robot. The effectiveness of the proposed control approach is validated through comparative experiments.

https://doi.org/10.1017/S0263574725102300 Published online by Cambridge University Press

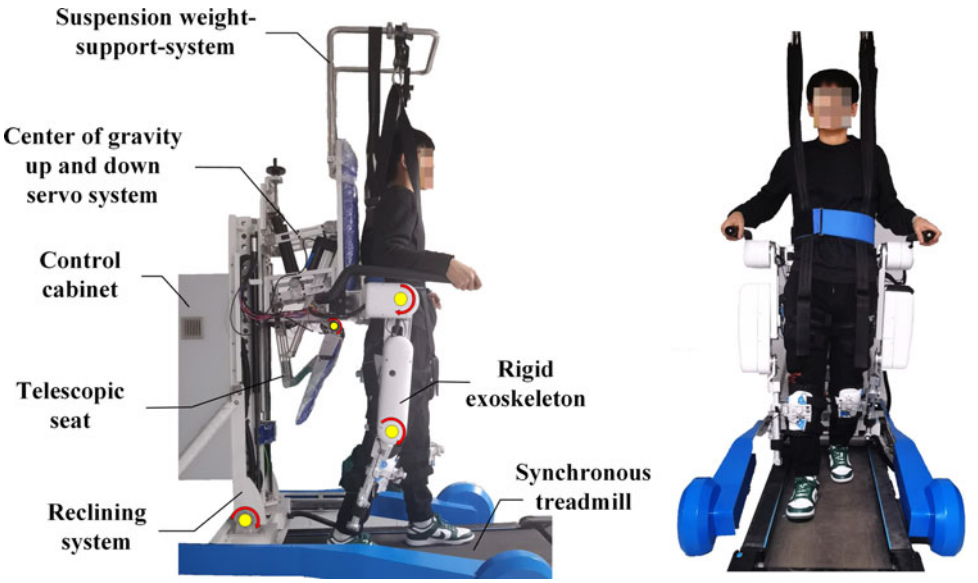


Figure 1. *Multi-posture lower limb rehabilitation robot prototype.*

2. Structural design of the multi-posture lower limb rehabilitation robot

Aiming to adequately address the multi-stage rehabilitation training needs of patients with lower-limb movement disorders (e.g., stroke and other neurological diseases), reduce the physical footprint of rehabilitation robots, reduce R&D costs, and enhance its rehabilitation capacity and efficiency, this paper presents a multi-posture lower-limb rehabilitation training robot capable of supine, seated, and standing postures. The robot comprises an exoskeleton, a telescopic seat, a tracking and lifting mechanism, a supine positioning mechanism, a weight-support system, and an active drive system. The exoskeleton mimics the physiological mechanics of the human thigh, calf, and foot, with rigid articulated connecting rods arranged in series. Paired with adjustable hip width, thigh length, and calf length mechanisms, it accommodates patients with diverse postures and body dimensions. The exoskeleton, in conjunction with the supine positioning mechanism, telescopic seat, and weight-support system [34], isolates multi-joint movements of the human lower limbs in the sagittal plane and tracks joint motion trajectories. The structural prototype of the multi-posture lower-limb rehabilitation training robot is depicted in Figure 1.

3. Human-exoskeleton coupling dynamic modeling

The exoskeleton of the rehabilitation robot is a rigid structure composed of serially connected rigid linkages. By comparison, the human lower-limb surface consists of flexible tissues (e.g., muscles and skin), while the internal skeleton is rigid. During robot use, the patient's lower limbs are connected to the exoskeleton via a human–machine contact interaction unit, typically a flexible strap. Thus, human–machine coupling establishes a complex, rigid-flexible coupled system during rehabilitation training. Furthermore, the coupling stiffness between the exoskeleton and the human body directly influences gait quality and comfort [35].

Prior studies [36, 37] often model the human–machine system as a single rigid body, assuming the exoskeleton leg is perfectly and rigidly attached to the lower limb. While this assumption simplifies mathematical modeling, it overlooks two key factors that restrict its practical applicability: (1) Joint center mechanical misalignment: The simplified rotational motion of robotic joints differs inherently from the complex elliptical trajectory of human knee joints. Even minor kinematic discrepancies can

https://doi.org/10.1017/S0263574725102300 Published online by Cambridge University Press

generate unexpected interaction forces at the human–robot interface. Zanotto et al.'s experiment [38] showed that a 20 mm thigh length mismatch resulted in a 15% increase in hip joint interaction torque during the mid-swing phase. Holistic equivalent models cannot capture such phenomena due to their inability to analyze local soft-tissue compliance at the human–robot interface. (2) Inertial parameter individual differences: These models rely on anthropometric average values for body segment inertial parameters (BSIPs), neglecting inter-individual variations in mass distribution, muscle tissue morphology, and limb geometry. Hwang et al. [37] demonstrated that using generic BSIPs (e.g., Dempster model) results in a root-mean-square error of 7.3 N m in joint torque estimation, underscoring the necessity for user-specific parameterization. In contrast to the holistic equivalence approach, the rigid-flexible coupling relationship between humans and machines is decomposed into segments for separate modeling. The force transfer mechanism in human–machine coupled interaction is analyzed.

3.1. Dynamics modeling of rehabilitation robot exoskeleton components

Regarding the exoskeleton of the rehabilitation robot, the following assumptions are made: (1) The exoskeleton consists of two rigid linkages, with the center of gravity located in the central symmetrical plane of the linkages; (2) the model is limited to motion in the sagittal plane; and (3) the robot leg and foot pedal are treated as a single rigid body. These assumptions streamline the analytical derivation of the Lagrangian dynamic equations, focusing on core kinematic–dynamic relationships while avoiding complexities arising from material flexibility or three-dimensional motion coupling. This approach aligns with standard practices in preliminary robot dynamics modeling, enabling systematic formulation of the baseline framework.

The dynamic equation is derived using the Lagrangian method. A coordinate system is defined with the hip joint center as the origin, where counterclockwise joint rotation is defined as positive. The dynamic equation of the exoskeleton under no-load conditions is

$$\tau_r = M_r\theta_r'' + C_r\theta_r' + G_r \tag{1}$$

where M_r, C_r, and G_r are the inertia, damping, and gravity 2×2 matrix of the exoskeleton, respectively; θ_r is the joint angle 2×1 vector of the exoskeleton hip and knee; and τ_r is the output torque 2×1 vector of the exoskeleton hip and knee joints. As depicted in Figure 2, within the base coordinate system, the centroid coordinates of the exoskeleton's thigh and calf segments are $Co_1^r(x_{c1}^r, y_{c1}^r)$ and $Co_2^r(x_{c2}^r, y_{c2}^r)$; the velocity of the exoskeleton's thigh and calf segments' centroid is $v_{c1}^r(x_{c1}^{r'}, y_{c1}^{r''})$ and $v_{c2}^r(x_{c2}^{r'}, y_{c2}^{r'})$, the formulations for calculating centroid coordinates and centroid velocity are provided in the Appendix. The total kinetic energy of the exoskeleton's thigh and calf segments is

$$\begin{aligned} T_r = {} & \frac{1}{2}m_1^r\left(L_{c1}^r\right)^2\left(\theta_1^r\right)^2 + \frac{1}{2}m_2^r\left(L_1\theta_1^{r'}\cos\theta_1^r + L_{c2}^r\left(\theta_1^{r'} + \theta_2^{r'}\right)\cos\left(\theta_1^r + \theta_2^r\right)\right)^2 \\ & + \frac{1}{2}m_2^r\left(-L_1\theta_1^{r'}\sin\theta_1^r - L_{c2}^r\left(\theta_1^{r'} + \theta_2^{r'}\right)\sin\left(\theta_1^r + \theta_2^r\right)\right)^2 + \frac{1}{2}J_{c1}^r\left(\theta_1^{r'}\right)^2 + \frac{1}{2}J_{c2}^r\left(\theta_2^{r'}\right)^2 \end{aligned} \tag{2}$$

where $m_1^r, m_2^r, L_1, L_{c1}^r, L_{c2}^r$, and g denote the mass of the exoskeleton thigh; the mass of the calf; the distance from the hip joint center of the thigh to the knee joint center; the distance from the hip joint center of the thigh to the center of mass of the thigh; the distance from the knee joint center of the calf to the center of mass of the calf; and the acceleration due to gravity, respectively.

Although the rigid-body and sagittal-plane assumptions facilitate basic dynamic modeling, they may introduce inaccuracies in scenarios involving flexible materials, three-dimensional gaits (e.g., pelvic tilt during turning), or compliant ground interactions (e.g., nonlinear foot-ground forces). As a foundational framework, future investigations will integrate flexible multi-body dynamics, three-dimensional motion coupling, and adaptive pedal compliance to improve clinical applicability.

The total potential energy of the exoskeleton's thigh and calf segments is

$$E_r = m_1^r g L_{c1}^r\cos\theta_1^r + m_2^r g\left(L_1\cos\theta_1^r + L_{c2}^r\cos\left(\theta_1^r + \theta_2^r\right)\right) \tag{3}$$

https://doi.org/10.1017/S0263574725102300 Published online by Cambridge University Press

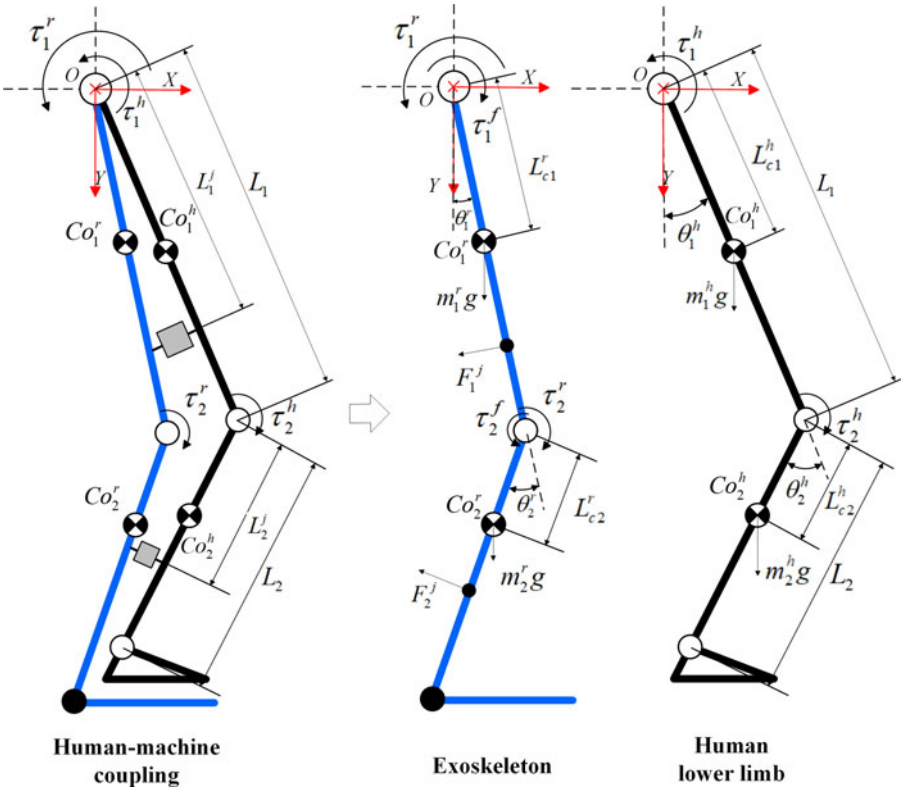


Figure 2. *Segmented equivalent model of human lower limb-exoskeleton.*

The Lagrange multiplier is

$$L = T_r - E_r \tag{4}$$

The dynamics equations of the exoskeleton derived using the Lagrangian method are:

$$\tau_i^r = \frac{\mathrm{d}}{\mathrm{d}t}\left(\frac{\partial L}{\partial \theta_i'}\right) - \frac{\partial L}{\partial \theta_i}, \quad i = 1, 2 \tag{5}$$

$$\begin{bmatrix} \tau_1^r \\ \tau_2^r \end{bmatrix} = \begin{bmatrix} M_{11}^r & M_{12}^r \\ M_{21}^r & M_{22}^r \end{bmatrix} \begin{bmatrix} \theta_1^{r''} \\ \theta_2^{r''} \end{bmatrix} + \begin{bmatrix} C_{11}^r & C_{12}^r \\ C_{21}^r & C_{22}^r \end{bmatrix} \begin{bmatrix} (\theta_1^{r'})^2 \\ (\theta_2^{r'})^2 \end{bmatrix} + \begin{bmatrix} D_{11}^r & D_{12}^r \\ D_{21}^r & D_{22}^r \end{bmatrix} \begin{bmatrix} \theta_1^{r'}\theta_2^{r'} \\ \theta_2^{r'}\theta_1^{r'} \end{bmatrix} + \begin{bmatrix} G_1^r \\ G_2^r \end{bmatrix} \tag{6}$$

Variable definitions for the equations are provided in the Appendix.

3.2. Biomechanical modeling of human lower limbs

For human lower limbs, higher model complexity correlates with more accurate kinematic descriptions [39]. However, increased model complexity leads to a drastic increase in computational load. Patients undergoing rehabilitation with robots predominantly perform sagittal-plane hip and knee joint motions. Thus, this study balances model accuracy against computational efficiency by omitting hip joint degrees of freedom (DOFs) in the coronal (adduction/abduction) and horizontal (internal/external rotation) planes, as well as all ankle joint DOFs (including sagittal dorsiflexion/plantar flexion and coronal varus/valgus). As a result, human lower limbs are modeled as a 2-DOF (two-degree-of-freedom) planar linkage.

https://doi.org/10.1017/S0263574725102300 Published online by Cambridge University Press

In the base coordinate system, the centroid coordinates of the thigh and calf are $Co_1^h(x_{c1}^h, y_{c1}^h)$ and $Co_2^h(x_{c2}^h, y_{c2}^h)$, respectively, and the velocities of the centroids of the thigh and calf are $v_{c1}^h(x_{c1}^{h'}, y_{c1}^{h'})$ and $v_{c2}^h(x_{c2}^{h'}, y_{c2}^{h'})$, respectively. The total kinetic energy of the system composed of the thigh and calf is

$$\begin{aligned} {}_h = &\frac{1}{2}m_1^h\left(L_{c1}^h\right)^2\left(\theta_1^h\right)^2 + \frac{1}{2}m_2^h\left(L_1\theta_1^{h'}\cos\theta_1^h + L_{c2}^h\left(\theta_1^{h'} + \theta_2^{h'}\right)\cos\left(\theta_1^h + \theta_2^h\right)\right)^2 \\ &+ \frac{1}{2}m_2^h\left(-L_1\theta_1^h\sin\theta_1^h - L_{c2}^h\left(\theta_1^{h'} + \theta_2^{h'}\right)\sin\left(\theta_1^h + \theta_2^h\right)\right)^2 + \frac{1}{2}J_{c1}^h\left(\theta_1^{h'}\right)^2 + \frac{1}{2}J_{c2}^h\left(\theta_2^{h'}\right)^2 \end{aligned} \tag{7}$$

where m_1^h, m_2^h, L_{c1}^h, and L_{c2}^h denote the mass of the human lower limb thigh; the mass of the calf; the distance from the hip joint center to the center of mass of the thigh; and the distance from the knee joint center to the center of massof the calf; the moment of inertia of the thigh about the hip joint; and the moment of inertia of the calf about the knee joint, respectively.

The total potential energy of the human thigh and calf segments is

$$E_h = m_1^h g L_{c1}^h\cos\theta_1^h + m_2^h g\left(L_1\cos\theta_1^h + L_{c2}^h\cos\left(\theta_1^h + \theta_2^h\right)\right) \tag{8}$$

The Lagrange multiplier is

$$L = T_h - E_h \tag{9}$$

The dynamic equation of the human lower limb derived using the Lagrangian method is

$$\tau_i^h = \frac{\mathrm{d}}{\mathrm{d}t}\left(\frac{\partial L}{\partial\theta_i'}\right) - \frac{\partial L}{\partial\theta_i}, \quad i = 1, 2 \tag{10}$$

$$\begin{bmatrix}\tau_1^h\\ \tau_2^h\end{bmatrix} = \begin{bmatrix}M_{11}^h & M_{12}^h\\ M_{21}^h & M_{22}^h\end{bmatrix}\begin{bmatrix}\theta_1^{h''}\\ \theta_2^{h''}\end{bmatrix} + \begin{bmatrix}C_{11}^h & C_{12}^h\\ C_{21}^h & C_{22}^h\end{bmatrix}\begin{bmatrix}\left(\theta_1^{h'}\right)^2\\ \left(\theta_2^{h'}\right)^2\end{bmatrix} + \begin{bmatrix}D_{11}^h & D_{12}^h\\ D_{21}^h & D_{22}^h\end{bmatrix}\begin{bmatrix}\theta_1^{h'}\theta_2^{h'}\\ \theta_2^{h'}\theta_1^{h'}\end{bmatrix} + \begin{bmatrix}G_1^h\\ G_2^h\end{bmatrix} \tag{11}$$

The specific meaning of the variables in the formula is shown in the Appendix.

3.3. Modeling of flexible contact interfaces in human-exoskeleton interaction

During predefined positional rehabilitation training with the robot, the mechanical leg length, hip joint spacing, and exoskeleton posture remain constant. The lower limb is secured to the exoskeleton, and relative motion between the limb and exoskeleton primarily arises from elastic deformation of muscle, skin, and straps. Mechanically, the rehabilitation robot's suspension-based weight-support system is not independent but forms an integrated support framework via connections between the backboard and exoskeleton components. As the servo system tracks the human body's vertical center of gravity movement, the suspension system ensures synchronous vertical motion, constraining trunk-robot relative displacement at the hardware level. To validate this mechanical coupling, the NOKOV motion capture system (accuracy: 0.1 mm) was used to collect 10 training trial datasets (Figure 3(a)), simultaneously measuring 3D coordinates of reference points on the human trunk, hip, knee, ankle, and corresponding robot markers. Experimental results (Figure 3(b)) show mean three-dimensional distance deviations of: Trunk reference point: 8.3587 mm, hip joint reference point: 9.3838 mm, knee joint reference point: 4.0963 mm, and ankle joint reference point: 4.4388 mm. These deviations represent 1.0%–1.4% of the experimental gait step length (600–800 mm), qualifying as negligible errors in kinematic analysis, indicating small human–machine relative motion at trunk and joint points, consistent with rigid coupling kinematics.

Based on the mechanical design (rigid structural integration) and experimental results (relative motion), this study assumes that during rehabilitation training, (1) the human torso and robot backplane form a kinematic unity (shared coordinate system). (2) The foot and exoskeleton foot are rigidly bound (hip/ankle joint coordinate centers coincide with exoskeleton joint centers). (3) Human–robot

https://doi.org/10.1017/S0263574725102300 Published online by Cambridge University Press

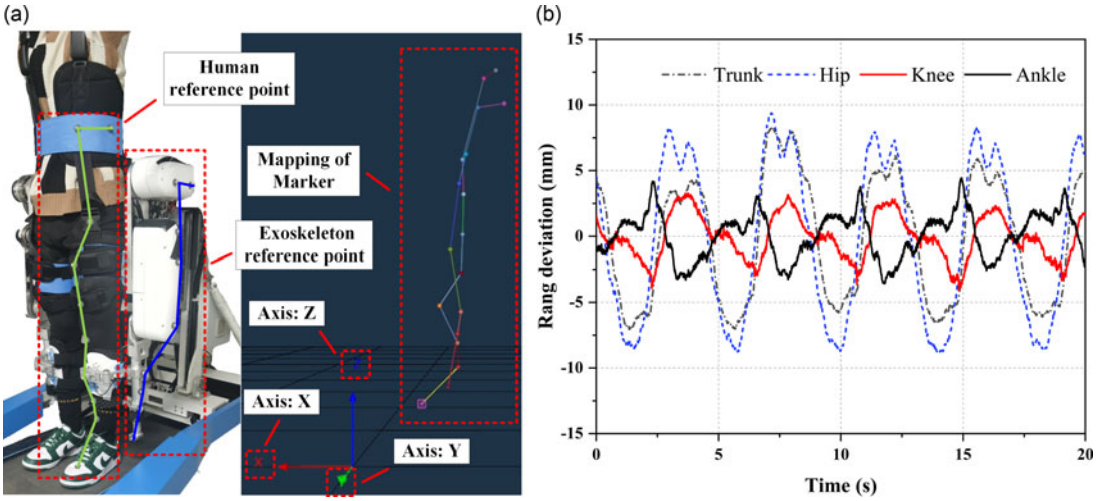


Figure 3. ***(a)*** *Human–robot reference point 3D motion trajectories during gait training (NOKOV motion capture),* ***(b)*** *quantitative analysis of three-dimensional distance deviations between human joints and robot reference points.*

relative displacement and interaction forces arise exclusively from elastic deformations in the contact area between straps and the body.

Prior studies (e.g., [40, 41]) simplify the human–exoskeleton interaction interface as rigid-body or spring-damper-connected two-rigid-body systems, neglecting the mechanical properties of soft tissues (skin, muscle, and flexible bandages). In contrast, our model adopts a layered composite structure to distinguish rigid components (human bones, exoskeleton) and flexible components (soft tissues, connectors). By introducing viscoelastic parameters to characterize energy dissipation in soft tissues, we reduce transmission errors caused by oversimplification (see Table I for detailed comparisons).

This explicit modeling of soft tissue mechanics and flexible contact interactions enables more accurate simulation of complex rehabilitation motions, surpassing the rigid-body assumptions in ref. [40] (which ignore soft tissue flexibility) and the limited joint-level focus in ref. [41] (which do not explicitly model soft tissue viscoelasticity). Our model dynamically adapts to changes in the patient's motor ability during rehabilitation, enhancing its applicability to real-world scenarios.

As illustrated in Figure 4, the skin and muscle on the human limb surface form a flexible contact layer S_2. Unlike the contact collision of two rigid bodies, the contact interface between the rehabilitation robot exoskeleton and the human body exhibits two regimes. The first regime involves the bottom support acting as the rigid exoskeleton's S_1 surface. The other is S_3 fixed by a flexible belt. The rigid and flexible properties of "B" and "E" are different, and there is an approximate non-contact between S_1 and S_2 in the process of motion, that is, $z_0 \geq 0$; and S_3 is always in contact with S_2, that is, $z_3 \equiv 0$. Therefore, this study treats human-limb–exoskeleton collision contact as flexible contact for modeling. Under the assumption of no collision impulse, contact loss is determined directly from position and velocity without considering impulsive dynamics. The interaction between human lower limbs and the exoskeleton is investigated in one-dimensional sagittal-plane collision contact, with other three-dimensional components neglected. Within the human–machine interaction contact system, the generated contact interaction force is dominated by contact and friction forces perpendicular to the leg direction. This study employs a first-order system to construct a flexible contact model. This modeling approach enables the separation of rigid-body dynamics in the human–machine coupled system from contact mechanics. The relative position and velocity of the human–machine system determine the contact interaction force, which is subsequently incorporated into the robot dynamics system as a known input.

https://doi.org/10.1017/S0263574725102300 Published online by Cambridge University Press

Table I. *Comparison of the proposed model with prior studies.*

Aspect	**Reference [40] (rigid-body model)**	**Reference [41] (two-rigid-body model)**	**The proposed model in this study**
Model structure	Single degree of freedom rigid body	Two-rigid-body system with spring-damper connection	Layered composite structure:– Rigid body part (bone, exoskeleton),– Flexible parts (skin, muscle, bandage)
Interactive modeling method	Torque balance equation (Considering Coulomb friction [40, Eq. (1)]	Impedance model (stiffness, damping [41, Eq. (6)]	Viscoelastic model of soft tissues + multi-point contact force (bandage)
Considered tissues	Ignoring soft tissues (assumes rigid connection)	Ignore soft tissue (focuses on joint-level interaction)	Explicitly models the viscoelasticity of skin/muscle and the flexibility of the bandage
Transmission error	High (rigid-body simplification)	Medium (spring-damper equivalence)	Low (integrated flexible contact mechanics)
Application scenario	Single-DOF exoskeleton swing motion	Multi-DOF exoskeleton gait adaptation	Complex motions with variable contact forces (adapts to the patient's motor ability during rehabilitation)

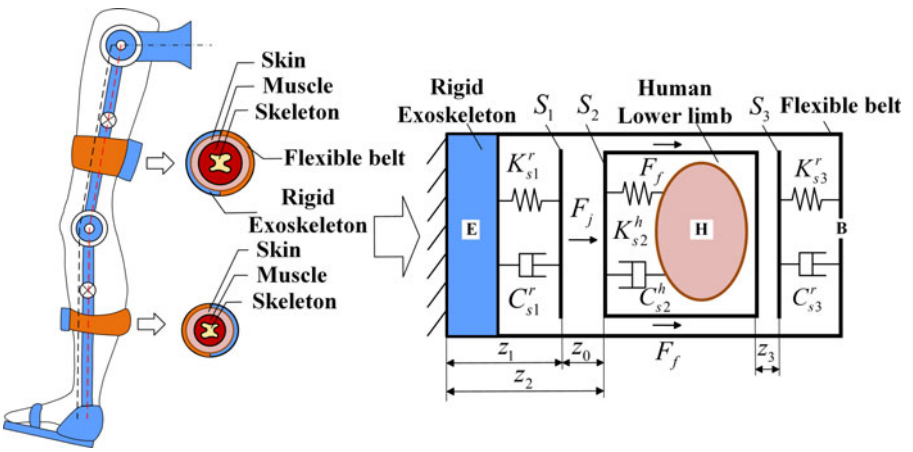


Figure 4. *Human-exoskeleton interaction contact model.*

The contact model mainly includes the exoskeleton rigid body part "E," the flexible belt part "B," the limb skeleton rigid body "H", the zero-mass contact surface S_1, S_2, and S_3, and three equivalent springs and three equivalent dampers. Variables z_1, z_2, z_3, and z_0 represent the position of the S_1 and S_2 contact surfaces and the distance between the contact surfaces, respectively. K^r_{s1}, K^r_{s3}, K^h_{s2}, C^r_{s1}, C^r_{s3}, and C^h_{s2} are the stiffness and damping coefficients of the S_1, S_3, and S_2 contact surfaces, respectively. As the human limb and exoskeleton contact interface are engaged via strapping, lateral friction acts on the limb in addition to the normal contact force F_f.

https://doi.org/10.1017/S0263574725102300 Published online by Cambridge University Press

In flexible contact modeling, the Coulomb friction model effectively characterizes the frictional force. Accounting for frictional effects, the human–robot interaction contact model (HRIF) is herein developed:

$$F_i = \begin{cases} K_1^d\left(v_i^r - v_i^h\right) + C_1^d\left(v_i^{r'} - v_i^{h'}\right) + f_{c,i}sign\left(v_i^{r'} - v_i^{h'}\right) + f_{s,i}\left(v_i^{r'} - v_i^{h'}\right), & z_0 > 0 \\ K_2^d\left(v_i^r - v_i^h\right) + C_2^d\left(v_i^{r'} - v_i^{h'}\right) + f_{c,i}sign\left(v_i^{r'} - v_i^{h'}\right) + f_{s,i}\left(v_i^{r'} - v_i^{h'}\right), & z_0 = 0 \end{cases}$$

$$K_1^d = \frac{K_{s3}^r K_{s2}^h}{K_{s3}^r + K_{s2}^h}, C_1^d = C_{s3}^r + C_{s2}^h$$

$$K_2^d = \frac{\left(K_{s1}^r + K_{s3}^r\right) K_{s2}^h}{K_{s1}^r + K_{s3}^r + K_{s2}^h}, C_2^d = \frac{C_{s1}^r C_{s3}^r}{C_{s1}^r + C_{s3}^r} + C_{s2}^h \tag{12}$$

In the formula, $F_i\sim, \sim i = 1, 2$ represent the human–machine interaction contact force at the thigh and calf, respectively. v_i^r, v_i^h represent the displacement of the exoskeleton and the human lower limb segments. $f_{c,i}$,$f_{s,i}$ represent the Coulomb friction coefficient and the viscous friction coefficient, respectively.

3.4. Integrated human-exoskeleton coupling model

Analysis of the rehabilitation robot's exoskeleton joint driving torque reveals that the joint torque output comprises three primary components: the torque required to drive the exoskeleton under ideal conditions τ_r, the torque required to drive the patient's lower limbs under perfect conditions τ_h, and the human–machine interaction force resulting from rigid-flexible coupling lossesτ_{hr}:

$$\tau = \tau_r + \tau_{hr} + \tau_h \tag{13}$$

Based on the dynamic equation of the rehabilitation robot's exoskeleton (formula (1)), parameter identification under no-load conditions determines the unknown parameters of the exoskeleton dynamic model to derive the torque required to drive the exoskeleton. Friction at the exoskeleton's actuated joints is influenced by multiple factors, exhibiting nonlinear dependence on joint velocity, which renders accurate linear modeling challenging. The rehabilitation robot employed in this study is equipped with a torque sensor at the joint output, enabling direct measurement of joint torque and indirect compensation for frictional interference. In subsequent control research, motor current measurements can estimate the torque output of the deactivated motor. The discrepancy between the joint's commanded torque and measured torque reveals the torque dissipated by friction, which is temporarily disregarded in this analysis. For human lower limbs, this study adopts the anthropometric mass proportion method from Anthropometric Reference Data [42] to determine thigh and calf mass ratios. By integrating the human lower limb equivalent dynamics equation with formula (11), the torque required to drive the limbs under ideal conditions is identified. The HRIF model characterizes human–machine coupling forces, and by transforming each component's torque into the exoskeleton's joint space, the human–machine coupled dynamic equation is ultimately derived:

$$M_r\theta_r'' + C_r\theta_r' + G_r\theta_r = \tau_r + \tau_{hr} + \tau_h \tag{14}$$

$$\tau_{hr} = Q_{hr}\left(C_i^h, K_i^h, C_i^r, K_i^r, f_{c,i}, f_{s,i}\right) \tag{15}$$

$$\tau_h = \Phi_r^T \Phi_h^{-T}\left(M_h\theta_h'' + C_h\theta_h' + G_h\right) \tag{16}$$

In the formula, $Q_{hr}(\,)$ represents the function of the parameters of the interactive contact model, Φ_h, Φ_r is the Jacobian matrix of the exoskeleton and the human lower limb.

4. Adaptive admittance control for lower limb rehabilitation robots

The patient's active force in human–machine interaction reflects motor ability and intention [43]. To ensure patient safety and comfort, the rehabilitation robot must adjust the mechanical leg's trajectory

https://doi.org/10.1017/S0263574725102300 Published online by Cambridge University Press

control according to the patient's motion intention. To avoid excessive compressive forces between the mechanical leg and human lower limbs – and thereby prevent injury – this study presents an adaptive admittance control strategy utilizing root mean square propagation (RMSprop) to dynamically adjust damping and stiffness parameters for compliance control.

In rehabilitation scenarios, the adaptive adjustment of admittance control parameters must simultaneously satisfy human–machine collaborative control's safety, real-time performance, and dynamic adaptability requirements [44]. Traditional gradient descent (SGD) with a fixed learning rate fails to address time-varying demands, while deep learning methods rely on offline training [45]. In contrast, RMSprop achieves dynamic learning rate scaling via exponential weighted averaging of gradient squares. The parameter update process will not cause system oscillation due to energy accumulation, ensuring safety. Compared to deep learning, RMSprop's low computational complexity meets the real-time constraint of the rehabilitation robot's 1-ms joint control cycle. Furthermore, as patients' motor function evolves during rehabilitation (e.g., joint angular velocity increasing from 0.1 rad/s to 0.8 rad/s), RMSprop's adaptive mechanism, via adjustable exponential weighting coefficients, flexibly balances historical and current gradients, enabling personalized adaptation to non-stationary force distributions [46]. Thus, RMSprop is selected as the adaptive adjustment algorithm for admittance control parameters.

In this study, the human–machine interaction force deviation is defined as a loss function, serving as a metric to evaluate human–machine interaction performance:

$$\Gamma\left(t\right) = \left\| F^m\left(t\right) - F_d\left(t\right) \right\|_2 \tag{17}$$

where F^m and F_d are the measured and expected values of the human-–exoskeleton interaction force. The damping parameter learning rate is defined as follows:

$$G_B^m = \gamma G_B^{m-1} + \left(1-\gamma\right) \cdot \left[\frac{\partial \Gamma^m\left(t\right)}{\partial B_d^m\left(t\right)} \right]^2 \tag{18}$$

The adaptive adjustment rate of the damping coefficient is derived:

$$B_d^{m+1}\left(t\right) = B_d^m\left(t\right) - \frac{\eta_B}{\sqrt{G_B^m + \varepsilon}} \cdot \frac{\partial \Gamma^m\left(t\right)}{\partial B_d^m\left(t\right)} \tag{19}$$

where γ represents the attenuation coefficient, η represents the learning rate, ε represents the numerical stability of the small constant, $\partial\Gamma^m(t)/\partial B_d^m(t)$ the calculation formula is

$$\frac{\partial \Gamma^m\left(t\right)}{\partial B_d^m\left(t\right)} = \frac{\partial f^m\left(t\right)}{\partial B_d^m\left(t\right)} \cdot \frac{\partial \Gamma^m\left(t\right)}{\partial f^m\left(t\right)} = \theta'^m\left(t\right) \frac{\partial \Gamma^m\left(t\right)}{\partial F^m\left(t\right)} \tag{20}$$

Similarly, the learning rate and adaptive adjustment rate of the stiffness coefficient are derived:

$$G_K^m = \gamma G_K^{m-1} + \left(1-\gamma\right) \cdot \left[\frac{\partial \Gamma^m\left(t\right)}{\partial K_d^m\left(t\right)} \right]^2 \tag{21}$$

$$K_d^{m+1}\left(t\right) = K_d^m\left(t\right) - \frac{\eta_K}{\sqrt{G_K^m + \varepsilon}} \cdot \frac{\partial \Gamma^m\left(t\right)}{\partial K_d^m\left(t\right)} \tag{22}$$

$$\frac{\partial \Gamma^m\left(t\right)}{\partial K_d^m\left(t\right)} = \frac{\partial f^m\left(t\right)}{\partial K_d^m\left(t\right)} \frac{\partial \Gamma^m\left(t\right)}{\partial f^m\left(t\right)} = \theta^m\left(t\right) \frac{\partial \Gamma^m\left(t\right)}{\partial F^m\left(t\right)} \tag{23}$$

Formula (12) quantifies the human–machine contact relationship, maps it to joint space, and establishes the mechanical impedance relationship during human–machine interaction as

$$f\left(t\right) = M\left(t\right)\theta''\left(t\right) + B\left(t\right)\theta'\left(t\right) + K\left(t\right)\theta\left(t\right) \tag{24}$$

To obtain $\partial\Gamma/\partial F_d^m(t)$, the idea of iterative learning is used to calculate [47]. The admittance system assumes that the human–machine interaction force in the initial static state is 0. On this basis, the state variables $x_1(t) = \theta(t), x_2(t) = x_1'(t), x_3'(t) = f(t)$ are taken. The output matrix between the system state and

https://doi.org/10.1017/S0263574725102300 Published online by Cambridge University Press

the output $y(t)$ is $C(t)$, and the direct transfer matrix is $D(t)$. The human–machine interaction force is treated as the system input. The state-space expression and output equation for the mechanical impedance in human–machine interaction are given as follows:

$$\begin{cases} x'(t) = A(t)x(t) + B(t)f(t) \\ y(t) = C(t)x(t) + D(t)f(t) \end{cases} \tag{25}$$

In the formula, $A(t)$ is the state matrix, $B(t)$ is the input matrix, and its specific form is

$$A(t) = \begin{bmatrix} 0 & 1 & 0 \\ -M^{-1}(t)K(t) & -M^{-1}(t)B(t) & 0 \\ 0 & 0 & 0 \end{bmatrix} \tag{26}$$

$$B(t) = \begin{bmatrix} 0 \\ M^{-1}(t) \\ 1 \end{bmatrix} \tag{27}$$

$$x(t) = \begin{bmatrix} x_1(t) \\ x_2(t) \\ x_3(t) \end{bmatrix} \tag{28}$$

Taking $f(t)$ as the control input, for the linear time-invariant system described by Eq. (25), the D-type learning control mechanism is adopted, and the update rule of human–machine interaction force is

$$f^m(t) = f^{m-1}(t) - \varsigma e_m(t) \tag{29}$$

In the formula, $e_m(t) = y'^m(t) - y'_d(t)$, ς satisfies:

$$\|I - \varsigma B(t)C(t)\|_\infty < 1 \tag{30}$$

where I is the identity matrix.

By updating the control input, that is, the interaction force, the deviation between the control output $y^m(t)$ and $y_d(t)$ is reduced. The deviation is also described by the loss function of Eq. (17), and it can be obtained:

$$f^m(t) = f^m(t) - \sigma \cdot \frac{\partial \Gamma^m(t)}{\partial F^m(t)} \tag{31}$$

By formulas (30) and (31), we obtain:

$$\frac{\partial \Gamma^m(t)}{\partial F^m(t)} = \frac{\varsigma}{\sigma}\left(y'^m(t) - y'_d(t)\right) \tag{32}$$

By substituting formula (32) into formula (19) and formula (22), and taking $\alpha = \varsigma/\sigma$, the adaptive rate of the damping coefficient and stiffness coefficient can be obtained:

$$B_d^{m+1}(t) = B_d^m(t) - \frac{\eta_B \alpha \theta'^m(t)}{\sqrt{G_B^m + \varepsilon}} \cdot \left(y'^m(t) - y'_d(t)\right) \tag{33}$$

$$K_d^{m+1}(t) = K_d^m(t) - \frac{\eta_K \alpha \theta^m(t)}{\sqrt{G_K^m + \varepsilon}} \cdot \left(y'^m(t) - y'_d(t)\right) \tag{34}$$

The inner-loop position controller is integrated with the outer-loop admittance controller. RMSprop is employed to optimize the admittance parameters, and the adaptive adjustment rates of the admittance controller's damping and stiffness parameters are designed to achieve human–machine cooperative motion control via interaction force. The framework of the double-loop control system is illustrated in Figure 5.

https://doi.org/10.1017/S0263574725102300 Published online by Cambridge University Press

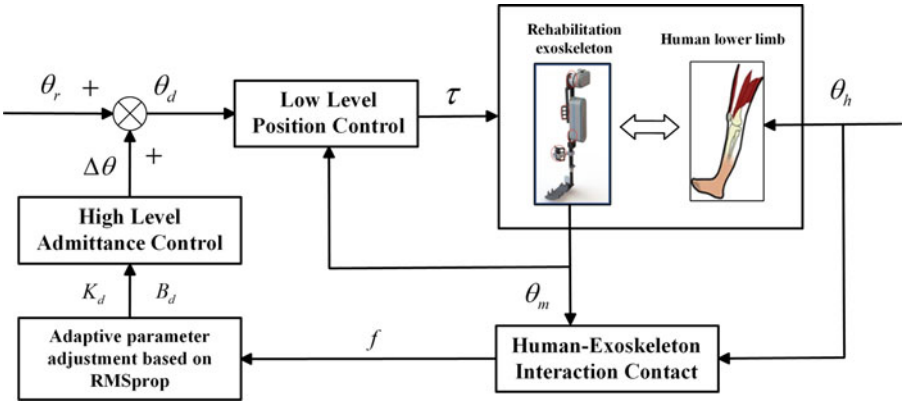


Figure 5. *Adaptive admittance control system framework.*

5. Experiment validation

5.1. Experimental identification of exoskeleton inertial parameters

The rehabilitation robot's exoskeleton model can be identified via conventional dynamic parameter identification following linearization. Linearization of the exoskeleton dynamic equation enables the derivation of rigid exoskeleton parameters. The linearized form of the dynamic equation is

$$\tau_r = M_r\theta_r'' + C_r\theta_r' + G_r = H\left(\theta_r'', \theta_r', \theta_r\right) X \tag{35}$$

where $H(\theta_r'', \theta_r', \theta_r)$ is the observation matrix and X is the inertial parameter matrix. A detailed explanation is given in the Appendix.

Under the no-load condition (i.e., considering only the exoskeleton's weight), the exoskeleton's motion excitation trajectory is input to the rehabilitation robot. This trajectory is parameterized using the FFS method [48] and optimized using the condition number criterion [49] and the particle swarm optimization algorithm [50]. The trajectory covers the rehabilitation training range of the hip joint (−30°, 60°) and knee joint (0°, 120°), ensuring effective excitation of the inertial parameters to be identified.

The high-precision MILLE encoder (6400 PPR) and torque sensor (range: 360 N m, resolution: 0.01 N m) were used. They collected data from the rehabilitation robot operating along the motion excitation trajectory, including hip and knee joint angles and joint output torque. The collected data were first smoothed and filtered to ensure data accuracy and reliability. The LOWESS method was employed for filtering, with the window size control parameter span set to 0.05, which preserved key motion features while suppressing noise.

The genetic algorithm [48, 49] was used to identify the inertial parameters. The relevant parameter settings were as follows: the initial population size was 1000 (with the optimal size determined via pre-test), the crossover probability was 0.8 (determined by referring to similar studies and adapted to the present model), the mutation probability was 0.01 (to balance convergence and diversity), and the maximum number of iterations was 1000 (pre-test verified the sufficiency of convergence). The static penalty function was used to constrain the reasonable range of the parameters to be identified. The objective function was the minimum of the error between the theoretical and measured torque, plus the minimum of the static penalty function.

Measurement data from 10 groups of excitation trajectory motions were recorded. Each group of trajectories differed in motion amplitude, frequency, or joint coupling relationship, thus covering richer motion modes and improving the robustness of parameter identification. The dynamic inertial parameter identification results for the rehabilitation robot's exoskeleton are shown in Table II.

With experimental baseline conditions unchanged, an exoskeleton motion trajectory is replanned based on the gait trajectory of healthy subjects and applied to the rehabilitation robot. Motion and torque data are collected from joint sensors. Concurrently, the theoretically determined model is employed for

https://doi.org/10.1017/S0263574725102300 Published online by Cambridge University Press

Table II. *Identification results of the exoskeleton.*

Parameter	Description	Value	Parameter	Description	Value
m_1^r	Thigh mass	3.0573 (kg)	m_2^r	Calf mass	2.6048 (kg)
L_1^r	Thigh length	458.3 (mm)	L_{c2}^r	Distance from the knee joint to the center of mass of the calf	216.5 (mm)
L_{c1}^r	Distance from the hip joint to the center of mass of the thigh	293.7 (mm)	J_2^r	Moment of inertia of the calf	4132 (kg mm^2)
J_1^r	Moment of inertia of the thigh	6254 (kg mm^2)			

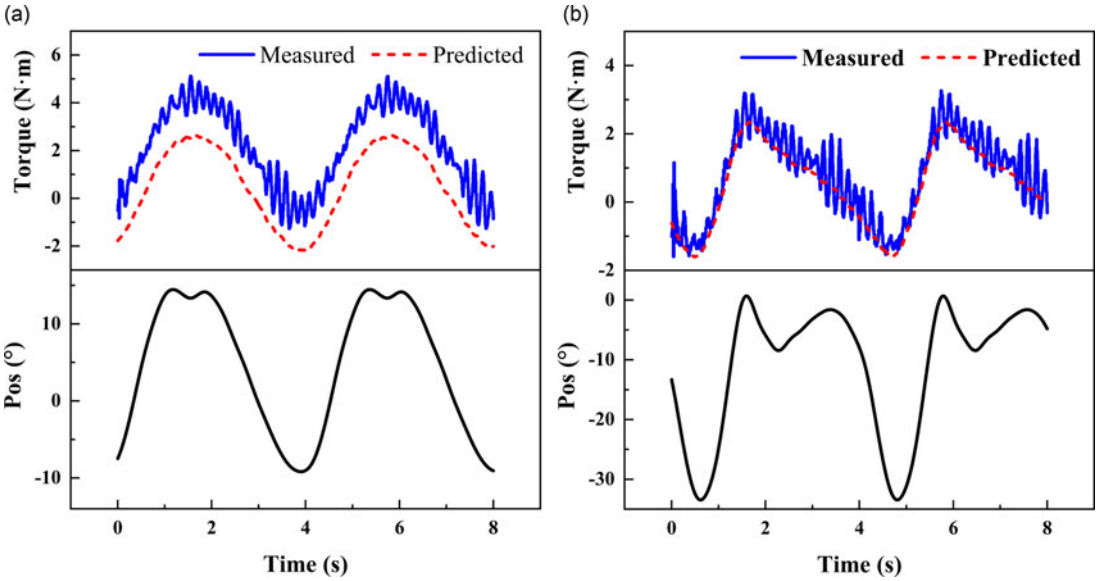


Figure 6. *Comparison of theoretical and experimental torque results for hip and knee joints. (a) Hip joint. (b) Knee joint.*

computation, and experimental values are compared with theoretical predictions. As shown in Figure 6, the predicted results are consistent with the overall trend of the sensor measurement results, but the measured values are greater than the expected values. To clarify the source of error, a zero-calibration test of the sensor was conducted before the experiment, and factors such as sensor accuracy and signal transmission interference were examined. It was determined that the offset arose from the sensor's zero offset. The correlation coefficients between the measured and theoretical values were further calculated to be 0.92, indicating a high correlation between the fluctuation patterns of the two, with no impact on the validity of the verification results.

5.2. Experimental identification of human lower limb inertial parameters

The standard human body attribute proportion method described in ref. [42] is a generic empirical model. However, due to individual differences in anthropometric parameters and body segment properties (such as height, body weight, segmental bone lengths (e.g., femur, tibia, and humerus), mass

https://doi.org/10.1017/S0263574725102300 Published online by Cambridge University Press

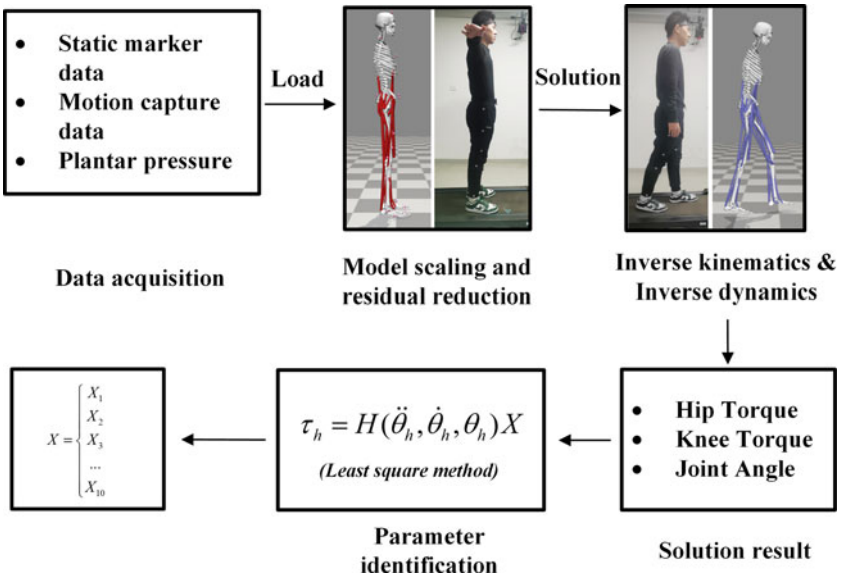


Figure 7. *Parameter identification workflow for the human lower extremity using OpenSim.*

distribution, muscle-fat ratio, joint morphology, and kinematic properties), significant errors may occur. OpenSim [51], a widely used biomechanical simulation software, performs inverse dynamics simulations of human walking using motion data and ground reaction forces. Its accuracy is highly validated in the literature and is widely recognized for reliability [52, 53].

Therefore, this paper collected the subject's motion capture marker and plantar pressure data. The collected data were filtered using a Butterworth low-pass filter (cutoff frequency: 6 Hz). The generic model was scaled in OpenSim based on the filtered marker data. The collected marker data included static data used to scale the generic model and adjust its proportions to match the subject's body dimensions and motion data used to solve inverse kinematics and inverse dynamics. By comparing the distances between the marker points of the generic model and those of the subject, the scaling ratio weights were adjusted, with the maximum error controlled to less than 2 cm and the root mean square error to less than 1 cm, thereby establishing the subject-specific model.

Then, using OpenSim's inverse kinematics and inverse dynamics analysis functions [54], the collected plantar pressure data were loaded to calculate the muscle force, joint force, and torque of the human lower limb model. Hip and knee joint angles (flexion–extension direction time series) and joint torque (torque time series) were exported from OpenSim, while body segment parameters (such as thigh mass, moment of inertia, centroid position, among others) following model scaling were derived. The obtained joint angle and torque data were used to extract the effective segment of the walking cycle (single support phase) for subsequent parameter identification; the segment parameters were compared with the anthropometric database [55] to verify that parameters such as thigh moment of inertia fell within the normal biomechanical range, ensuring the model's validity.

Finally, based on the joint torque and joint angle data, the least squares method was used to identify the parameters of the human lower limb dynamic model. The covariance matrix of the output parameters was obtained during the identification process. By taking the square roots of the diagonal elements of the matrix, the standard deviation (SD) of each inertial parameter was derived, quantifying the uncertainty in the parameter estimation (a smaller SD indicates better stability of the model fit to the experimental data). The detailed implementation procedure is illustrated in Figure 7, with the identification results tabulated in Table III.

https://doi.org/10.1017/S0263574725102300 Published online by Cambridge University Press

Table III. *Identification results of the human lower limb.*

Description	Parameter	Value	SD	Description	Parameter	Value	SD
Thigh mass	m_1^h	9.532 (kg)	0.125	Calf mass	m_2^h	3.283 (kg)	0.087
Thigh length	L_1^h	458.3 (mm)	2.31	Moment of inertia of the calf	J_2^h	31,164 (kg mm^2)	243.6
Distance from the hip joint to the center of mass of the thigh	L_{c1}^h	309.3 (mm)	1.85	Distance from the knee joint to the center of mass of the calf	L_{c2}^h	238.7 (mm)	1.52
Moment of inertia of the thigh	J_1^h	128,983 (kg·mm^2)	562.4				

5.3. Parameter identification of the human–machine interaction contact model

Drawing on the parameter identification framework in ref. [56] and other related studies, the experiment was designed based on the contact characteristics addressed in this study, and the experiment was conducted using the multi-posture lower limb rehabilitation robot platform. The subject was a 26-year-old healthy adult male, with a height of 170 cm and a weight of 66 kg. The subject's hip and knee joints were well matched with the mechanical leg. A one-dimensional force sensor was installed at the human–machine interaction contact module of the thigh and calf (i.e., at the connection between S1 and the exoskeleton E). The sensor parameters are as follows: range: 360 N, resolution: 0.01 N, nonlinearity: ±0.02% F.S, repeatability: ±0.02% F.S, and hysteresis: ±0.02% F.S. The rehabilitation robot adopted a passive training mode to drive the subject to move along the preset gait trajectory. The subject did not actively exert force; instead, the mechanical leg drove the human lower limbs to simulate human–machine interaction in real rehabilitation scenarios.

Reflective markers were attached to the subject's lower limbs and mechanical legs, and the NOKOV motion capture system was used to acquire real-time motion information of the human limbs and the rehabilitation robot exoskeleton (sampling frequency: 100 Hz). Motion and interaction contact force information were recorded synchronously during the experiment. A total of 10 sets of data were collected, with the first eight sets used as the experimental group (for parameter identification) and the last two sets as the verification group (for model verification). The LOWESS method was first used for filtering, with the window size control parameter span set to 0.05, which preserved key motion features and suppressed noise.

The ranges of the model's three equivalent spring and damping coefficients are determined based on their material properties and related research, as presented in Table IV. Among them, S1 (polypropylene medical guard plate) is a hard material with small deformation and a narrow parameter variation range. S2 (human tissue), composed of soft structures such as muscle and skin, exhibits significant deformation and slow recovery after loading, resulting in a wide damping parameter range. The elasticity of S3 (flexible strap, nylon material) is between that of the first two; it can be stretched but has a limited deformation range.

To address the complexity of the human–machine interaction contact model and account for the overall context, this study uses the genetic algorithm – suitable for nonlinear and multi-parameter optimization problems – to identify the parameters of the human–machine interaction contact model. The relevant parameters are set as follows: initial population size = 500, crossover probability = 0.8, mutation probability = 0.02, constraint conditions are set according to the previously determined parameter ranges, and maximum number of iterations = 1000 (convergence criterion: fitness change<1e-4 for 50 consecutive generations). The objective function is the minimum error between the theoretical and measured interaction forces.

The identification results of the three equivalent springs and damping coefficients are presented in Table V. These results were verified using data from the verification group. Figure 8 shows the verification group's model prediction and actual measurement results over two random motion cycles. By

https://doi.org/10.1017/S0263574725102300 Published online by Cambridge University Press

Table IV. *Reference range of parameters of the interactive contact model.*

Contact position	Stiffness (N/m)	Damping (N·s/m)	Based on literature/standards
S1	1000–2000	8–18	Conversion according to the characteristics of polypropylene material in ref. [57]
S2	1000–4000	10–40	Contact stiffness and damping range of human lower limb soft tissue in ref. [58]
S3	500–1500	10–40	Research results of nylon binding band for traditional Chinese medicine in ref. [59]

Table V. *Parameter identification results of the interactive contact model.*

	Stiffness (N/m)			Damping(N s/m)			Friction	
Parameter	K_1^r	K_2^h	K_3^r	C_1^r	C_2^h	C_3^r	f_c	f_s
Calf	1368.55	1030.34	1013.39	10.01	10.98	10.55	0.99	8.11
Thigh	1619.93	1027.68	1000.23	10.00	15.94	11.00	1.0	8.46

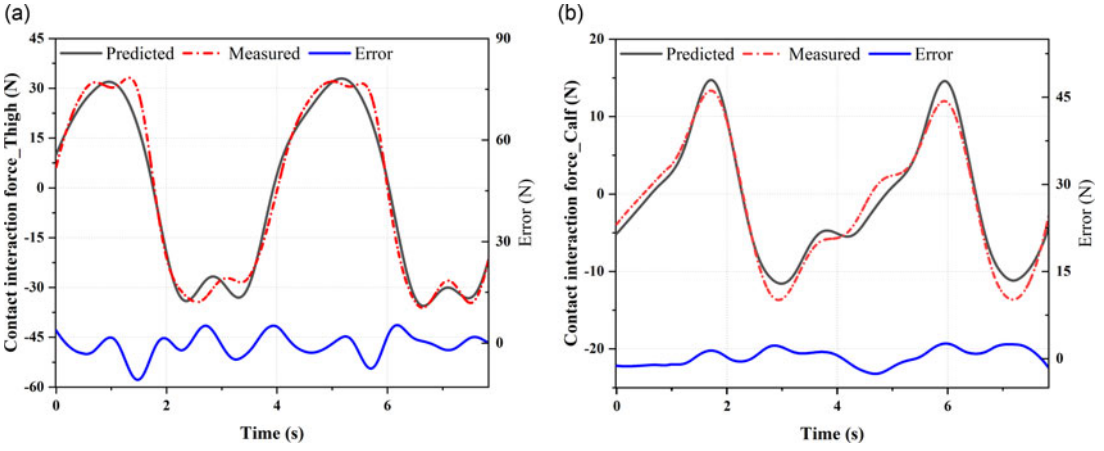


Figure 8. *Validation of human–computer interaction contact model parameter results.*

comparing the force–time curves of the theoretical and measured results in the figure, the two trends are found to be generally consistent. The maximum root mean square errors (RMSEs) of the verification results for the thigh and calf are 2.3187 and 1.4461 N, respectively. This error range falls within the valid error range of similar research results (RMSE/maximum interaction force $\leq$ 10%, ref. [56]), confirming the validity of the identification results.

5.4. Experimental validation of adaptive admittance control

Based on the results of the previous parameter identification experiments, the numerical solution of the human–machine coupled dynamic equation excluding interaction losses is derived. The interaction force is then fed into the adaptive admittance control model to obtain trajectory deviations induced by interaction forces. To validate the control performance and interaction comfort of human–machine cooperative motion with the adaptive admittance controller, a comparative experiment is designed in this study.

https://doi.org/10.1017/S0263574725102300 Published online by Cambridge University Press

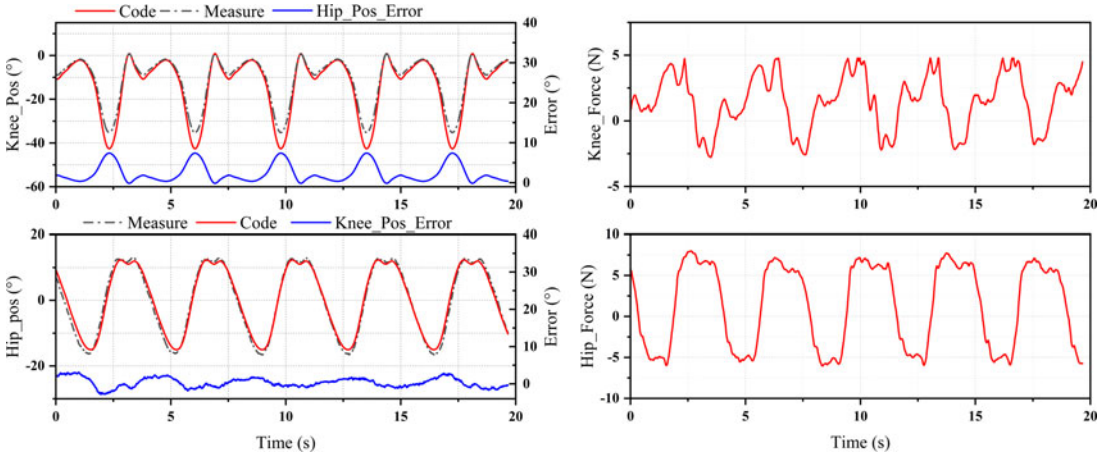


Figure 9. *Experimental results of the adaptive admittance controller.*

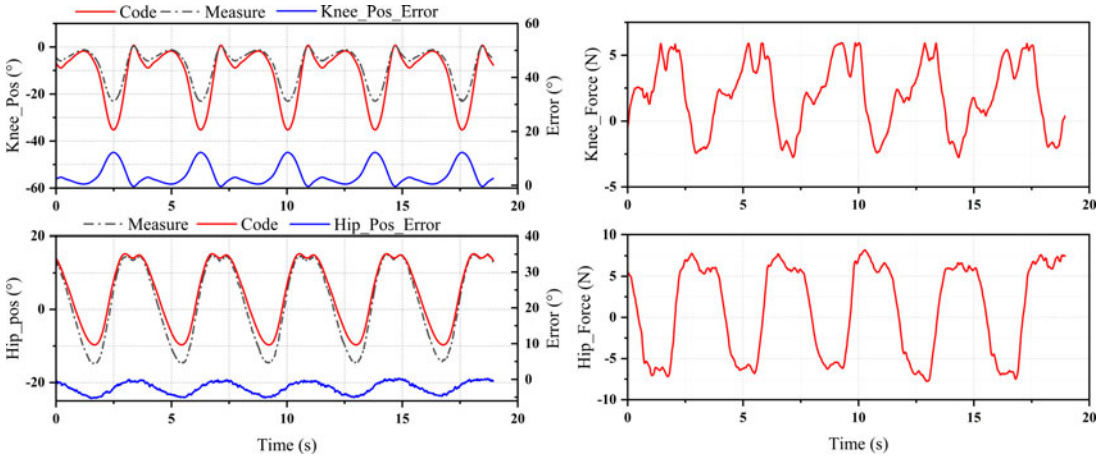


Figure 10. *Experimental results of the fixed admittance controller.*

Subjects were secured to the rehabilitation robot and walked at a constant speed on a treadmill. The NOKOV motion capture system collected human lower limb motion data, while the rehabilitation robot synchronously recorded exoskeleton joint trajectory outputs and interaction forces.

Figure 9 illustrates the hip and knee joint motion trajectories and human–machine interaction forces under adaptive admittance parameter adjustment. Figure 10 depicts the same metrics with fixed admittance parameters. Figures 9 and 10 show four complete and continuous gait cycles [60] randomly selected during walking.

The experimental data comparisons are presented in Tables VI and VII. The relative reduction rate is calculated as

$$\text{Relative reduction rate} = \left(1 - \frac{\text{Adaptive}}{\text{Fixed}}\right) \times 100 \tag{36}$$

Table VI demonstrates that the adaptive controller reduces the maximum hip and knee joint angle errors by 40.9% and 39.4%, respectively, and mean angle errors by 53.1% and 38.6% compared to the fixed parameter controller. For human–exoskeleton interaction forces (Table VII), the maximum thigh and calf forces decrease by 2.8% and 19.4%, while mean forces reduce by 7.0% and 22.2%. These results confirm the adaptive controller's superiority in improving joint angle consistency and minimizing interaction forces, with clear baseline comparisons (fixed parameter controller) provided for each metric.

https://doi.org/10.1017/S0263574725102300 Published online by Cambridge University Press

Table VI. *Comparison of joint angle errors.*

Metrics	Group	Hip joint (°)	Knee joint (°)
Maximum angle error	Fixed parameter control	5.307438	12.20716
	Adaptive control	3.1346935	7.395271
	Relative reduction rate	**40.9%**	**39.4%**
Mean angle error	Fixed parameter control	2.35574	3.9353
	Adaptive control	1.1054	2.4160
	Relative reduction rate	**53.1%**	**38.6%**

The use of boldface is to precisely emphasize the relative improvement effects of adaptive control on two types of metrics (joint angle errors and human - exoskeleton interaction forces).

Table VII. *Comparison of human-exoskeleton interaction forces.*

Metrics	Group	Thigh force (N)	Calf force (N)
Maximum force	Fixed parameter control	8.2032531	5.959276
	Adaptive control	7.972655	4.8044682
	Relative reduction rate	**2.8%**	**19.4%**
Mean force	Fixed parameter control	5.3391	2.8144
	Adaptive control	4.9674	2.1904
	Relative reduction rate	**7.0%**	**22.2%**

The use of boldface is to precisely emphasize the relative improvement effects of adaptive control on two types of metrics (joint angle errors and human - exoskeleton interaction forces).

6. Conclusion

This study presents a multi-posture lower limb rehabilitation robot system designed to address multi-stage rehabilitation requirements. By analyzing human–machine coupling interactions during rehabilitation training, the human–machine contact relationship is quantified using a flexible contact approach, enabling dynamic decoupling of interaction forces and motion trajectory deviations. Unlike conventional human–machine integrated equivalent modeling approaches, the human–machine system is decomposed into subsystems, and a human–machine coupled dynamic model accounting for contact losses in human–machine interaction is developed.

An admittance controller incorporating adaptive RMSprop rate adjustment is developed. Leveraging a low-level position controller, a double-loop control system for the lower limb rehabilitation robot is designed to realize adaptive compliance control.

The inertial parameters of the exoskeleton of the lower-limb rehabilitation robot and the human lower limb were identified through experiments. The inertial and contact model parameters of each human–machine system component were determined. A comparative experiment was conducted to verify the adaptive compliance controller. The results show that, compared with the fixed-compliance-parameter controller, the adaptive compliance controller significantly improves trajectory consistency, with the maximum joint angle error reduced by more than 48.4% and the maximum human–machine interaction force decreased by more than 21.4%. This advantage directly enhances the safety and effectiveness of rehabilitation training. The notable reduction in trajectory error can mitigate the risk of secondary injury caused by movement deviation. At the same time, the decrease in interaction force can improve patients' training adaptability and ensure safety during long-term rehabilitation.

Compared with the research by Lu et al. [19], this study further elucidates the mechanism of human–machine interaction contact in lower-limb rehabilitation training and provides new insights for reducing human–machine interaction force, enhancing comfort and coordination, and mitigating the risk of secondary injury. Compared with existing fixed-parameter control [31] or simplified human–machine models [41], the "human–machine coupling dynamic model considering contact loss" proposed in this study overcomes the limitations of traditional integrated modeling and achieves dynamic decoupling of

https://doi.org/10.1017/S0263574725102300 Published online by Cambridge University Press

force and trajectory deviation. The "adaptive root mean square propagation rate adjustment admittance controller" developed based on this model addresses the static setting of compliance parameters and enables dynamic and personalized rehabilitation control. The above results provide key technical support for rehabilitation robots' human–machine collaboration theory and advance the field from "passive assistance" to "active adaptation".

However, there are three key limitations in this study:

1. Limitation in subject scope: The methods were validated only in healthy adults, and their efficacy for stroke patients with motor dysfunctions (e.g., spastic hemiplegia, balance disorders) remains untested. Pathological individual differences (e.g., muscle spasticity, joint contracture) may disrupt the controller's ability to adapt to dynamic human–machine interaction patterns, affecting control strategies' adaptability in clinical use.
2. Limitation in algorithm robustness evaluation: While effective in standard scenarios, the controller's robustness under extreme conditions (sudden patient resistance, external disturbances) has not been tested. This unevaluated robustness may lead to inadequate real-time adjustment under such conditions, potentially limiting its real-time adaptability in practice.
3. Insufficiency in clinical validation: The evaluation focused on kinematic and force interaction metrics but lacked a systematic assessment of long-term outcomes (motor function recovery, gait symmetry, and quality of life). These long-term outcomes are critical for determining the practical clinical utility of the methods, as they directly reflect the actual benefits for rehabilitation.

In the future, clinical trials for different patient cohorts, algorithm optimization, and long-term efficacy tracking can be conducted to address the above limitations. On this basis, the human–machine coupling dynamics modeling and adaptive compliance control method proposed in this study can be extended to other fields of wearable robots, such as exoskeleton assistance devices and robots for individuals with disabilities, and provide a general technical framework for solving safety and comfort issues in human–machine collaboration.

Author contribution. Conceptualization, Chao Gao and Chang Wang; methodology, Chao Gao; software, Chao Gao; validation, Chang Wang, Hui Li, Jianhua Zhang, Xinpeng Du, and Jianjun Zhang; formal analysis, Chang Wang; investigation, Hui Li; resources, Xinpeng Du; data curation, Jianhua Zhang; writing—original draft preparation, Chao Gao; writing—review and editing, Chang Wang; visualization, Chang Wang; supervision, Jianhua Zhang; project administration, Jianjun Zhang; funding acquisition, Hui Li.

Financial support. This work was supported by the National Natural Science Foundation of National Key R&D Program of China (Grant No. 2023YFB4706100) and National Natural Science Foundation of China (Grant No. U23A20338).

Competing interests. The authors declare no conflicts of interest exist.

Ethical approval. Not applicable.

References

[1] K. S. Tan, J. D. Pandian, L. Liu, K. Toyoda, T. W. H. Leung, S. Uchiyama, S. Kuroda, N. C. Suwanwela, S. Aaron, H. M. Chang and N. Venketasubramanian, "Stroke in Asia," *Cerebrovasc. Dis. Extra* **14**(1), 58–75 (2024). doi: 10.1159/000538928.

[2] L.-D. W. W.-J. Tu and S. W. G. o. C. S. S. Report, "China stroke surveillance report 2021," *Mil. Med. Res.* **10**(1), 33 (2023). doi: 10.1186/s40779-023-00463-x.

[3] A. D. Banyai and C. Brişan, "Robotics in physical rehabilitation: Systematic review," *Healthcare* **12**(17), (2024). doi: 10.3390/healthcare12171720.

[4] D. Han, "Application effect of rehabilitation robots in rehabilitation of limb movement disorders based on neural network algorithms," *SLAS Technology* **32**, 100277 (2025). doi: 10.1016/j.slast.2025.100277.

[5] R. Hong, B. Li, Y. Bao, L. Liu and L. Jin, "Therapeutic robots for post-stroke rehabilitation," *Med. Rev.* **4**(1), 55–67 (2024). doi: 10.1515/mr-2023-0054.

https://doi.org/10.1017/S0263574725102300 Published online by Cambridge University Press

[6] P. K. Tam, N. Tang, N. S. B. Kamsani, T. Y. Yap, I. Coffey-Aladdin, S. M. Goh, J. P. P. Tan, Y. C. Lui, R. L. Lee, R. Suresh and E. Chew, "Overground robotic exoskeleton vs conventional therapy in inpatient stroke rehabilitation: Results from a pragmatic, multicentre implementation programme," *J. Neuroeng. Rehab.* **22**(1), 3 (2025). doi: 10.1186/s12984-024-01536-1.

[7] Y.-H. Park, D.-H. Lee and J.-H. Lee, "A comprehensive review: Robot-assisted treatments for gait rehabilitation in stroke patients," *Medicina (Mex.)* **60**(4), 620 (2024). doi: 10.3390/medicina60040620.

[8] X. Zhang, Z. Yue and J. Wang, "Robotics in lower-limb rehabilitation after stroke," *Behav Neurol* **2017**, 3731802 (2017). doi: 10.1155/2017/3731802.

[9] A. Rodriguez-Fernandez, J. Lobo-Prat and J. M. Font-Llagunes, "Systematic review on wearable lower-limb exoskeletons for gait training in neuromuscular impairments," *J. Neuroeng. Rehabil.* **18**(1), 22 (2021). doi: 10.1186/s12984-021-00815-5.

[10] F. Bettella, S. Tortora, E. Menegatti, N. Petrone and A. D. Felice, "A scoping review on lower limb exoskeleton actuation's description and characteristics," *Robotica* **43**, 1–18 (2025). doi: 10.1017/s0263574725000220.

[11] R. S. CalabrÒ, G. Sorrentino, A. Cassio, D. Mazzoli, E. Andrenelli, E. Bizzarini, I. Campanini, S. M. Carmignano, S. Cerulli, C. Chisari, V. Colombo, S. Dalise, C. FundarÒ, V. Gazzotti, D. Mazzoleni, M. Mazzucchelli, C. Melegari, A. Merlo, G. Stampacchia, P. Boldrini, S. Mazzoleni, F. Posteraro, P. Benanti, E. Castelli, F. Draicchio, V. Falabella, S. Galeri, F. Gimigliano, M. Grigioni, S. Mazzon, F. Molteni, G. Morone, M. Petrarca, A. Picelli, M. Senatore, G. Turchetti and D. Bonaiuti, "Robotic-assisted gait rehabilitation following stroke: A systematic review of current guidelines and practical clinical recommendations," *Eur. J. Phys. Rehab. Med.* **57**(3), (2021). doi: 10.23736/s1973-9087.21.06887-8.

[12] X. Li, F. Fang, R. Li and Y. Zhang, "Functional brain controllability alterations in stroke," *Front. Bioeng. Biotechnol.* **10**, 925970 (2022). doi: 10.3389/fbioe.2022.925970.

[13] C. Zich, N. S. Ward, N. Forss, S. Bestmann, A. J. Quinn, E. Karhunen and K. Laaksonen, "Post-stroke changes in brain structure and function can both influence acute upper limb function and subsequent recovery," *NeuroImage: Clin.* **45**, 103754 (2025). doi: 10.1016/j.nicl.2025.103754.

[14] J. Li, Y. Zhou, M. Dong, X. Rong and R. J. R. Jiao, "Clinically oriented ankle rehabilitation robot with a novel R-2U-PSRR mechanism," *Robotica* **41**(1), 277–291 (2023).

[15] M. Bouri, E. Abdi, H. Bleuler, F. Reynard and O. Deriaz. "Lower Limbs Robotic Rehabilitation Case Study with Clinical Trials." **In:** *New Trends in Medical and Service Robots: Challenges and Solutions* (2014) pp. 31–44.

[16] S. Jezernik, G. Colombo, T. Keller, H. Frueh and M. Morari, "Robotic orthosis lokomat: A rehabilitation and research tool," *Neuromodul.: Technol. Neural Interface* **6**(2), 108–115 (2003). doi: 10.1046/j.1525-1403.2003.03017.x.

[17] Y. Feng, H. Wang, T. Lu, V. Vladareanuv, Q. Li and C. Zhao, "Teaching training method of a lower limb rehabilitation robot," *Int. J. Adv. Robot Syst.* **13**(2), (2017). doi: 10.5772/62445.

[18] X. Wang, H. Wang, X. Hu, Y. Tian, M. Lin, H. Yan, J. Niu and L. Sun, "Adaptive direct teaching control with variable load of the lower limb rehabilitation robot (LLR-II)," *Machines* **9**(8), 142 (2021). doi: 10.3390/machines9080142.

[19] H. Lu and HWang, "Human–machine coupling dynamics modeling and active compliance control of lower limb rehabilitation robot," *J. Mech. Eng.* **58**(7), 32–43 (2022).

[20] A. Kapsalyamov, S. Hussain, R. Goecke, N. A. T. Brown and P. K. Jamwal, "Customized stiffness control strategy for a six-bar linkage-based gait rehabilitation robot," *Robotica* **42**(10), 3398–3415 (2024). doi: 10.1017/s0263574724001425.

[21] D. Centeno-Barreda, S. Salazar-Cruz, R. López-Gutiérrez, Y. Rosales-Luengas and R. J. R. Lozano, "Lower limb exoskeleton for gait rehabilitation with adaptive nonsingular sliding mode control," *Robotica* **42**(11), 3819–3838 (2024).

[22] Z. Li, H. Wei, H. Zhang and C. Liu, "A variable admittance control strategy for stable and compliant human–robot physical interaction," *IEEE Robot. Autom. Lett.* **10**(2), 1138–1145 (2025). doi: 10.1109/lra.2024.3519885.

[23] J. Sun, F. Hu, K. Gao, F. Gao, C. Ma and J. J. R. Wang, "Research and experiment on active training of lower limb based on five-bar mechanism of man-machine integration system," *Robotica* **42**(5), 1453–1475 (2024).

[24] P. Zhang, J. Zhang and A. J. R. Elsabbagh, "Fuzzy radial-based impedance controller design for lower limb exoskeleton robot," *Robotica* **41**(1), 326–345 (2022).

[25] Y. Yang, J. Yin, W. Qi, Z. Li, Z. Zhou, Z. Liu and J. J. R. Xu, "Optimization and synthesis on the dynamics performance of the tensioning and relaxing wearable system in a novel knee exoskeleton using co-simulation," *Robotica* **42**(11), 3918–3933 (2024).

[26] J. Zhou, S. Yang and Q. Xue, "Lower limb rehabilitation exoskeleton robot: A review," *Adv. Mech. Eng.* **13**(4), 16878140211011862 (2021). doi: 10.1177/16878140211011862.

[27] Y. Zhu, Q. Wu, B. Chen, Z. Zhao and C. Liang, "Physical human–Robot interaction control of variable stiffness exoskeleton with sEMG-based torque estimation," *IEEE Trans. Ind. Inform.* **19**(10), 10601–10612 (2023). doi: 10.1109/tii.2023.3240749.

[28] J. Sun, E. H. Kramer and J. Rosen, "A safety-focused admittance control approach for physical human–Robot interaction with rigid multi-arm serial link exoskeletons," *IEEE/ASME Trans. Mechatron.* **30**(1), 414–425 (2025). doi: 10.1109/tmech.2024.3389046.

[29] C. Wang and J. Zhao, "Based on human-like variable admittance control for human–robot collaborative motion," *Robotica* **41**(7), 2155–2176 (2023).

[30] G. Aguirre-Ollinger, J. E. Colgate, M. A. Peshkin and A. Goswami, "Design of an active one-degree-of-freedom lower-limb exoskeleton with inertia compensation," *Int. J. Robot. Res.* **30**(4), 486–499 (2010). doi: 10.1177/0278364910385730.

[31] L. Chen, C. Wang, X. Song, J. Wang, T. Zhang and X. Li, "Dynamic trajectory adjustment of lower limb exoskeleton in swing phase based on impedance control strategy," *Proc. Inst. Mech. Eng., Part I: J. Syst. Control Eng.* **234**(10), 1120–1132 (2020). doi: 10.1177/0959651820932026.

[32] J. Schmidhuber, "A local learning algorithm for dynamic feedforward and recurrent networks," *Connect Sci.* **1**(4), 403–412 (2007). doi: 10.1080/09540098908915650.

https://doi.org/10.1017/S0263574725102300 Published online by Cambridge University Press

[33] J. Chen and P. I. Ro, "Variable admittance control in sliding mode for robust physical human–Robot interaction," *Appl. Sci.* **13**(20), (2023). doi: 10.3390/app132011219.

[34] L. A. Rodrigues and R. S. Gonçalves, "Development of a novel body weight support system for gait rehabilitation," *Robotica* **41**(4), 1275–1294 (2023).

[35] M. Shafiei and S. Behzadipour, "The effects of the connection stiffness of robotic exoskeletons on the gait quality and comfort," *J. Mech. Robot.* **12**(1), 011007 (2020). doi: 10.1115/1.4044841.

[36] X. Liang, Y. Yan, W. Wang, T. Su, G. He, G. Li and Z.-G. Hou, "Adaptive human–Robot interaction torque estimation with high accuracy and strong tracking ability for a lower limb rehabilitation robot," *IEEE/ASME Trans. Mechatron.* **29**(6), 4814–4825 (2024). doi: 10.1109/tmech.2024.3394491.

[37] B. Hwang and D. Jeon, "A method to accurately estimate the muscular torques of human wearing exoskeletons by torque *sensors*," *Sensors* **15**(4), 8337–8357 (2015). doi: 10.3390/s150408337.

[38] D. Zanotto, Y. Akiyama, P. Stegall and S. K. Agrawal, "Knee joint misalignment in exoskeletons for the lower extremities: Effects on user's gait," *IEEE Trans. Robot.* **31**(4), 978–987 (2015). doi: 10.1109/tro.2015.2450414.

[39] D. Maita and G. Venture. "Influence of the Model's Degree of Freedom on Human Body Dynamics Identification," **In:** *Proceedings of the 2013 35th Annual International Conference of the IEEE Engineering in Medicine and Biology Society (EMBC)* (2013) pp. 4609–4612.

[40] H.-T. Tran, H. Cheng, X. Lin, M.-K. Duong and R. Huang, "The relationship between physical human-exoskeleton interaction and dynamic factors: Using a learning approach for control applications," *Sci. China Inf. Sci.* **57**(12), 1–13 (2014). doi: 10.1007/s11432-014-5203-8.

[41] R. Huang, H. Cheng, J. Qiu and J. Zhang, "Learning physical human–Robot interaction with coupled cooperative primitives for a lower exoskeleton," *IEEE Trans. Autom. Sci. Eng.* **16**(4), 1566–1574 (2019). doi: 10.1109/tase.2018.2886376.

[42] C. Fryar, M. Carroll, Q. Gu, J. Afful and C. J. V. Ogden, Anthropometric reference data for children and adults: United States, 2015–2018, **36**, 1–44 (2021).

[43] C. Zou, C. Zeng, R. Huang, Z. Peng, J. Zhang and H. Cheng, "Online gait learning with assist-as-needed control strategy for post-stroke rehabilitation exoskeletons," *Robotica* **42**(2), 319–331 (2024).

[44] K. Almaghout, B. Tarvirdizadeh, K. Alipour and A. J. R. Hadi, "RBF neural network-based admittance PD control for knee rehabilitation robot," *Robotica* **40**(12), 4512–4534 (2022).

[45] A. Arefeen and Y. Xiang, "Artificial neural network-based control of powered knee exoskeletons for lifting tasks: Design and experimental validation," *Robotica* **42**(9), 2949–2968 (2024). doi: 10.1017/s0263574724001206.

[46] A. Rospawan, C.-C. Tsai and C.-C. Hung, "Two-layer intelligent learning control using output recurrent fuzzy neural long short-term memory broad learning system with RMSprop," *IEEE Access* **13**, 34334–34349 (2025). doi: 10.1109/access.2025.3543867.

[47] Y. Li and S. S. Ge, "Impedance learning for robots interacting with unknown environments," *IEEE Trans. Control Syst. Trans.* **22**(4), 1422–1432 (2014). doi: 10.1109/tcst.2013.2286194.

[48] R. Losantos, M. Montiel, R. Mustata, F. Zorrilla and L. Valiño, "Parameter characterization of HTPEMFC using numerical simulation and genetic algorithms," *Int. J. Hydrogen Energy* **47**(7), 4814–4826 (2022). doi: 10.1016/j.ijhydene.2021.11.084.

[49] D. Ostaszewicz and K. Rogowski, "Application of genetic algorithms for strejc model parameter tuning," *Electronics* **13**(18), 3652 (2024). doi: 10.3390/electronics13183652.

[50] P. Suraj, L. Wu, S. Guru and R. Buyya, A particle swarm optimization (PSO)-based heuristic for scheduling workflow applications in cloud computing environments (2012).

[51] A. Rajagopal, C. L. Dembia, M. S. DeMers, D. D. Delp, J. L. Hicks and S. L. Delp, "Full-body musculoskeletal model for muscle-driven simulation of human gait," *IEEE Trans. Biomed. Eng.* **63**(10), 2068–2079 (2016). doi: 10.1109/tbme.2016.2586891.

[52] A. S. Arnold, S. Salinas, D. J. Hakawa and S. L. Delp, "Accuracy of muscle moment arms estimated from MRI-based musculoskeletal models of the lower extremity," *Comput. Aided Surg.* **5**(2), 108–119 (2010). doi: 10.3109/10929080009148877.

[53] Ø. Sandbakk, C. L. Dembia, A. Silder, T. K. Uchida, J. L. Hicks and S. L. Delp, "Simulating ideal assistive devices to reduce the metabolic cost of walking with heavy loads," *PLos One* **12**(7), e0180320 (2017). doi: 10.1371/journal.pone.0180320.

[54] J. Wei, S. Zhang and J. J. R. Zhang, "Biofusion design and parameter optimization for a novel passive assisted knee exoskeleton robot based on eight-bar mechanism," *Robotica* **42**(6), 27 (2024).

[55] D. A. Winter, *Biomechanics and Motor Control of Human Movement* (iomechanics and Motor Control of Human Movement, 1987).

[56] Y. Yan, Z. Chen, C. Huang, L. Chen and Q. Guo, "Human-exoskeleton coupling dynamics in the swing of lower limb," *Appl. Math. Model.* **104**, 439–454 (2022). doi: 10.1016/j.apm.2021.12.007.

[57] J. Mo, L. Zeng, Y. Liu, L. Ma, C. Liu, S. Xiang and G. Cheng, "Mechanical properties and damping capacity of polypropylene fiber reinforced concrete modified by rubber powder," *Constr. Build. Mater.* **242**, 118111 (2020). doi: 10.1016/j.conbuildmat.2020.118111.

[58] M. J. Kang and H. H. Yoo, "In vivo viscoelastic properties of human thigh under compression estimated by experimental results obtained with pendulum test," *Int. J. Precis. Eng. Manuf.* **18**(9), 1253–1262 (2017). doi: 10.1007/s12541-017-0147-8.

[59] J. Cholewicki, A. S. Lee, N. P. Reeves and D. C. Morrisette, "Comparison of trunk stiffness provided by different design characteristics of lumbosacral orthoses," *Clin. Biomech.* **25**(2), 110–114 (2010). doi: 10.1016/j.clinbiomech.2009.10.010.

[60] W. Yin, W. Zhu, H. Gao, X. Niu, C. Shen, X. Fan and C. Wang, "Gait analysis in the early stage of parkinson's disease with a machine learning approach," *Front. Neurol.* **15**, 1472956 (2024). doi: 10.3389/fneur.2024.1472956.

https://doi.org/10.1017/S0263574725102300 Published online by Cambridge University Press

Appendix

$$\begin{cases} x_{c1}^{r} = L_{c1}^{r} \sin\theta_1^{r} \\ y_{c1}^{r} = L_{c1}^{r} \cos\theta_1^{r} \\ x_{c2}^{r} = L_1 \sin\theta_1^{r} + L_{c2}^{r} \sin\left(\theta_1^{r} + \theta_2^{r}\right) \\ y_{c2}^{r} = L_1 \cos\theta_1^{r} + L_{c2}^{r} \cos\left(\theta_1^{r} + \theta_2^{r}\right) \end{cases} \tag{37}$$

$$\begin{cases} x_{c1}^{r'} = L_{c1}^{r} \cos\theta_1^{r} \cdot \theta_1^{r'} \\ y_{c1}^{r'} = -L_{c1}^{r} \sin\theta_1^{r} \cdot \theta_1^{r'} \\ x_{c2}^{r'} = L_1 \cos\theta_1^{r} \cdot \theta_1^{r'} + L_{c2}^{r} \cos\left(\theta_1^{r} + \theta_2^{r}\right) \cdot \left(\theta_1^{r'} + \theta_2^{r'}\right) \\ y_{c2}^{r'} = -L_1 \sin\theta_1^{r} \cdot \theta_1^{r'} - L_{c2}^{r} \sin\left(\theta_1^{r} + \theta_2^{r}\right) \cdot \left(\theta_1^{r'} + \theta_2^{r'}\right) \end{cases} \tag{38}$$

$$\begin{aligned} &M_{11}^{r} = m_1^{r}\left(L_{c1}^{r}\right)^2 + m_2^{r}\left(L_{c2}^{r}\right)^2 + m_2^{r}\left(L_1\right)^2 + 2m_2^{r}L_1L_{c2}^{r}\cos\left(2\theta_1^{r} + \theta_2^{r}\right) + J_1^{r}; \\ &M_{12}^{r} = m_2^{r}\left(L_{c2}^{r}\right)^2 + m_2^{r}L_1L_{c2}^{r}\cos\left(2\theta_1^{r} + \theta_2^{r}\right); \\ &M_{21}^{r} = m_2^{r}\left(L_{c2}^{r}\right)^2 + m_2^{r}L_1L_{c2}^{r}\cos\left(2\theta_1^{r} + \theta_2^{r}\right); \\ &M_{22}^{r} = m_2^{r}\left(L_{c2}^{r}\right)^2 + J_2^{r}; C_{11}^{r} = 0; C_{12}^{r} = -m_2^{r}L_1L_{c2}^{r}\sin\theta_1^{r}; \\ &C_{21}^{r} = m_2^{r}L_1L_{c2}^{r}\sin\theta_2^{r}; C_{22}^{r} = 0; D_{11}^{r} = -2m_2^{r}L_1L_{c2}^{r}\sin\theta_1^{r}; \\ &D_{12}^{r} = D_{21}^{r} = D_{22}^{r} = 0; G_2^{r} = -m_2^{r}gL_{c2}^{r}\sin\left(\theta_1^{r} + \theta_2^{r}\right); \\ &G_1^{r} = -m_1^{r}gL_{c1}^{r}\sin\theta_1^{r} - m_2^{r}gL_{c2}^{r}\sin\left(\theta_1^{r} + \theta_2^{r}\right) - m_2^{r}gL_1\sin\theta_1^{r}; \\ &J_{c1}^{r} = I_{z1}^{r} + I_{z2}^{r} + m_1^{r}\left(L_{c1}^{r}\right)^2 + m_2^{r}\left(L_{c2}^{r}\right)^2 + m_2^{r}\left(L_1^{r}\right)^2; \\ &J_{c2}^{r} = I_{z2}^{r} + m_2^{r}\left(L_{c2}^{r}\right)^2; \end{aligned} \tag{39}$$

$$\begin{cases} x_{c1}^{h} = L_{c1}^{h} \sin\theta_1^{h} \\ y_{c1}^{h} = L_{c1}^{h} \cos\theta_1^{h} \\ x_{c2}^{h} = L_1 \sin\theta_1^{h} + L_{c2}^{h} \sin\left(\theta_1^{h} + \theta_2^{h}\right) \\ y_{c2}^{h} = L_1 \cos\theta_1^{h} + L_{c2}^{h} \cos\left(\theta_1^{h} + \theta_2^{h}\right) \end{cases} \tag{40}$$

$$\begin{cases} x_{c1}^{h'} = L_{c1}^{h} \cos\theta_1^{h} \cdot \theta_1^{h'} \\ y_{c1}^{h'} = -L_{c1}^{h} \sin\theta_1^{h} \cdot \theta_1^{h'} \\ x_{c2}^{h'} = L_1 \cos\theta_1^{h} \cdot \theta_1^{h'} + L_{c2}^{h} \cos\left(\theta_1^{h} + \theta_2^{h}\right) \cdot \left(\theta_1^{h'} + \theta_2^{h'}\right) \\ y_{c2}^{h'} = -L_1 \sin\theta_1^{h} \cdot \theta_1^{h'} - L_{c2}^{h} \sin\left(\theta_1^{h} + \theta_2^{h}\right) \cdot \left(\theta_1^{h'} + \theta_2^{h'}\right) \end{cases} \tag{41}$$

$$\begin{aligned} &M_{11}^{h} = m_1^{h}\left(L_{c1}^{h}\right)^2 + m_2^{h}\left(L_{c2}^{h}\right)^2 + m_2^{h}\left(L_1\right)^2 + 2m_2^{h}L_1L_{c2}^{h}\cos\left(2\theta_1^{h} + \theta_2^{h}\right) + J_1^{h}; \\ &M_{12}^{h} = m_2^{h}\left(L_{c2}^{h}\right)^2 + m_2^{h}L_1L_{c2}^{h}\cos\left(2\theta_1^{h} + \theta_2^{h}\right); \\ &M_{21}^{h} = m_2^{h}\left(L_{c2}^{h}\right)^2 + m_2^{h}L_1L_{c2}^{h}\cos\left(2\theta_1^{h} + \theta_2^{h}\right); \\ &M_{22}^{h} = m_2^{h}\left(L_{c2}^{h}\right)^2 + J_2^{h}; C_{11}^{h} = 0; C_{12}^{h} = -m_2^{h}L_1L_{c2}^{h}\sin\theta_1^{h}; \\ &C_{21}^{h} = m_2^{h}L_1L_{c2}^{h}\sin\theta_2^{h}; C_{22}^{h} = 0; D_{11}^{h} = -2m_2^{h}L_1L_{c2}^{h}\sin\theta_1^{h}; \\ &D_{12}^{h} = D_{21}^{h} = D_{22}^{h} = 0; G_2^{h} = -m_2^{h}gL_{c2}^{h}\sin\left(\theta_1^{h} + \theta_2^{h}\right); \\ &G_1^{h} = -m_1^{h}gL_{c1}^{h}\sin\theta_1^{h} - m_2^{h}gL_{c2}^{h}\sin\left(\theta_1^{h} + \theta_2^{h}\right) - m_2^{h}gL_1\sin\theta_1^{h}; \\ &J_{c1}^{h} = I_{z1}^{h} + I_{z2}^{h} + m_1^{h}\left(L_{c1}^{h}\right)^2 + m_2^{h}\left(L_{c2}^{h}\right)^2 + m_2^{h}\left(L_1^{h}\right)^2; \\ &J_{c2}^{h} = I_{z2}^{h} + m_2^{h}\left(L_{c2}^{h}\right)^2; \end{aligned} \tag{42}$$

https://doi.org/10.1017/S0263574725102300 Published online by Cambridge University Press

where I_{z1}^h, I_{z2}^h, I_{z1}^r, and I_{z2}^r are the rotational inertias of the thigh segment of the human lower limb about the hip joint, the thigh segment of the exoskeleton about the hip joint, the calf segment of the human lower limb about the knee joint, and the calf segment of the exoskeleton about the knee joint, respectively.

$$\Phi^j = \begin{bmatrix} -L_1^j \sin\left(\theta_1^j\right) - L_2^j \sin\left(\theta_1^j + \theta_1^j\right) & -L_2^j \sin\left(\theta_1^j + \theta_1^j\right) \\ L_1^j \cos\left(\theta_1^j\right) + L_2^j \cos\left(\theta_1^j + \theta_1^j\right) & L_2^j \cos\left(\theta_1^j + \theta_1^j\right) \end{bmatrix} \tag{43}$$

$$H = \begin{bmatrix} H_{11} & H_{12} & H_{13} & H_{14} & H_{15} & H_{16} & H_{17} & H_{18} & H_{19} & H_{10} \\ H_{21} & H_{22} & H_{23} & H_{24} & H_{25} & H_{26} & H_{27} & H_{28} & H_{29} & H_{20} \end{bmatrix} \tag{44}$$

$$\begin{aligned} &H_{11} = \theta_1^{j''}; H_{12} = \cos\left(2\theta_1^j + \theta_2^j\right)\theta_1^{j''}; H_{13} = \theta_2^{j''}; \sim \\ &\sim H_{14} = \cos\left(2\theta_1^j + \theta_2^j\right)\theta_2^{j''}; H_{15} = \left(\theta_1^{j'}\right)^2; H_{16} = \sin\left(\theta_1^j\right)\left(\theta_2^{j'}\right)^2; \\ &H_{17} = H_{18} = \theta_1^{j'}\theta_2^{j'}; H_{19} = g\sin\left(\theta_1^j\right); H_{10} = g\sin\left(\theta_1^j + \theta_2^j\right); \\ &H_{21} = \theta_1^{j''}; H_{22} = \theta_1^{j''}\cos\left(2\theta_1^j + \theta_2^j\right); H_{23} = \theta_1^{j''}; \\ &H_{24} = \left(\theta_1^{j'}\right)^2 \sin\left(\theta_2^j\right); H_{25} = \left(\theta_1^{j'}\right)^2; H_{26} = H_{27} = \theta_1^{j'}\theta_2^{j'}; \sim \\ &\sim H_{27} = \sin\left(\theta_2^j\right)\left(\theta_1^{j'}\right)^2; H_{28} = g\sin\left(\theta_1^j + \theta_2^j\right); H_{29} = H_{20} = 0; \end{aligned} \tag{45}$$

$$X = \begin{bmatrix} X_{11} & X_{12} & X_{13} & X_{14} & X_{15} & X_{16} & X_{17} & X_{18} & X_{19} & X_{10} \\ X_{21} & X_{22} & X_{23} & X_{24} & X_{25} & X_{26} & X_{27} & X_{28} & X_{29} & X_{20} \end{bmatrix}^T \tag{46}$$

$$\begin{aligned} &X_{11} = m_1^j\left(L_{c1}^j\right)^2 + m_2^j\left(L_{c2}^j\right)^2 + m_2^j\left(L_1^j\right)^2 + J_1^j; X_{12} = 2m_2^j L_{c2}^j L_1^j; \\ &X_{13} = m_2^j\left(L_{c2}^j\right)^2; X_{14} = m_2^j L_{c2}^j L_1^j; X_{15} = 0; X_{16} = -m_2^j L_{c2}^j L_1^j; \\ &X_{17} = -2m_2^j L_{c2}^j L_1^j; X_{18} = 0; X_{19} = -m_1^j L_{c1}^j - m_2^j L_1^j; \\ &X_{10} = -m_2^j L_{c2}^j; X_{21} = m_2^j\left(L_{c2}^j\right)^2; X_{22} = X_{24} = m_2^j L_{c2}^j L_1^j; \\ &X_{23} = m_2^j\left(L_{c2}^j\right)^2 + J_2^j; X_{25} = X_{26} = X_{27} = X_{29} = X_{20} = 0; \\ &X_{28} = -m_2^j L_{c2}^j; \end{aligned} \tag{47}$$

Cite this article: C. Gao, C. Wang, H. Li, J. Zhang, X. Du and J. Zhang (2025). "Human–machine coupling dynamics modeling and adaptive admittance control of lower limb rehabilitation robot", Robotica **43**, 3419–3441. https://doi.org/10.1017/S0263574725102300

https://doi.org/10.1017/S0263574725102300 Published online by Cambridge University Press